Redox Synergy: Enhancing Gas Sensing Stability in 2D Conjugated Metal–Organic Frameworks via Balancing Metal Node and Ligand Reactivity

Xiaoli Yan, Jie Chen, Xi Su, Jingwen Zhang, Chuanzhe Wang, Hanwen Zhang, Yi Liu,* Lei Wang, Gang Xu,* and Long Chen*

Abstract: Two-dimensional conjugated metal–organic frameworks (2D *c*-MOFs) have emerged as promising candidates in gas sensing, owing to their tunable porous structure and conductivity. Nevertheless, the reported gas sensing mechanisms heavily relied on electron transfer between metal nodes and gas molecules. Normally, the strong interaction between the metal sites and target gas molecule would result poor recovery and thus bad recycling property. Herein, we propose a redox synergy strategy to overcome this issue by balancing the reactivity of metal sites and ligands. A 2D *c*-MOF, $Zn_3(HHTQ)_2$, was prepared for nitrogen dioxide (NO_2) sensing, which was constructed from active ligands (hexahydroxyl-tricycloquinazoline, HHTQ) and inactive transition-metal ions (Zn^{2+}). Substantial characterizations and theoretical calculations demonstrated that by utilizing only the redox interactions between ligands and NO_2, not only high sensitivity and selectivity, but also excellent cycling stability in NO_2 sensing could be achieved. In contrast, control experiments employing isostructural 2D *c*-MOFs with Cu/Ni metal nodes exhibited irreversible NO_2 sensing. Our current work provides a new design strategy for gas sensing materials, emphasizing harnessing the redox activity of only ligands to enhance the stability of MOF sensing materials.

*T*wo-dimensional conjugated metal–organic frameworks (2D *c*-MOFs) typically consist of *ortho*-substituted (NH_2, OH, SH, or SeH) conjugated organic ligands and redox-active metal centers. These components combine to form a 2D layered structure through coordination bonds and tailored with exceptional properties.[1–4] They not only inherit the advantages of traditional metal–organic frameworks (MOFs), such as porosity and tunable structures, but also manifest intrinsic electrical conductivity. As a result, 2D *c*-MOFs have shown promising applications in chemiresistive sensors, electrocatalysis, capacitors, among others.[5–8] Chemically, the charge carrier conduction mechanism of 2D *c*-MOFs could be divided into *through-bond* and *through-space*.[9] The former focuses on improving bonding between metal ions and ligands to achieve stronger charge delocalization, particularly through the π-d conjugated hybrid orbitals, while the latter targets non-covalent interactions among organic moieties, such as π–π stacking. Subtle variations in carrier concentration along these two transmission paths, induced by external factors like light, electricity, or gas atmosphere, can result in significant alterations in the conductivity of 2D *c*-MOF.[10,11] Therefore, by the utilization of multivalent metal ion nodes, 2D *c*-MOFs have garnered attention in the realm of gas sensing, especially at room temperature.[11–21] Typically, the metal nodes of 2D *c*-MOFs are regarded as highly active sites for gas binding (Scheme 1a).[11] Nonetheless, the gas sensing mechanism, reliant on electron transfer between metal nodes and gas molecules, poses the risk of disrupting the coordination bonds, potentially compromising the framework's structural integrity during gas sensing. Furthermore, numerous multivalent metal ions, such as Cu and Ni, hold a strong affinity for gas molecules, impeding gas desorption from the framework during the gas sensing process. This inevitably results in prolonged recovery time and may hinder the sensing material from returning to its initial state, which constrains its cyclic response capabilities and severely limits the practical application.[14–16]

Within the architectural matrix of MOFs, the ligand-centered coordination spheres often exhibit a more expan-

[*] Dr. X. Yan, Prof. Y. Liu, Prof. L. Wang
Shenzhen Key Laboratory of Polymer Science and Technology,
Guangdong Research Center for Interfacial Engineering of Functional Materials, College of Materials Science and Engineering,
Shenzhen University,
Shenzhen 518060 (China)
E-mail: liuyiacee@szu.edu.cn

Dr. X. Yan, Prof. L. Wang
College of Physics and Optoelectronic Engineering,
Shenzhen University,
Shenzhen 518060 (China)

J. Chen, C. Wang, Prof. G. Xu
State Key Laboratory of Structural Chemistry, Fujian Provincial Key
Laboratory of Materials and Techniques toward Hydrogen Energy,
Fujian Institute of Research on the Structure of Matter, Chinese
Academy of Sciences,
Fuzhou, Fujian 350108, P. R. China
E-mail: gxu@fjirsm.ac.cn

X. Su, J. Zhang, H. Zhang, Prof. L. Chen
State Key Laboratory of Supramolecular Structure and Materials,
College of Chemistry, Jilin University,
Changchun 130012 (China)
E-mail: longchen@jlu.edu.cn
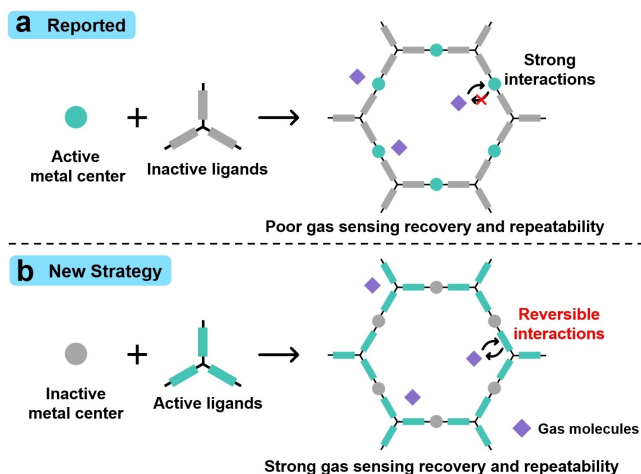
Scheme 1. (a) Illustration of 2D *c*-MOF sensing materials constructed with metal nodes as the sensing active sites. (b) Illustration of 2D c-MOF sensing materials constructed with bridging ligand as sensing active sites.

sive void space in comparison to the metal node environments. This spatial arrangement is advantageous as it permits a degree of structural flexibility when the ligands engage in interactions with gaseous molecules, resulting in minimal perturbation to the overall framework stability. Furthermore, the ligands can be strategically embellished with a diverse array of organic functional groups. Such modifications are instrumental in modulating the binding affinity and selectivity for various gas molecules, thereby enhancing the efficiency of adsorption and desorption processes during sensing processes. To overcome the above-mentioned issues in 2D *c*-MOF sensing materials, a potential strategy is to design sensing active sites on bridging ligands rather than on metal nodes (Scheme 1b).

To validate our hypothesis, we designed and synthesized a new 2D *c*-MOF, denoted as $Zn_3(HHTQ)_2$, which is constructed from NO_2 innocent Zn^{2+} transition metal ions and an active heteroaromatic ligand, 2,3,7,8,12,13-hexahydroxytricyclo-quinazoline (HHTQ). HHTQ possesses multiple unsaturated C=N bonds, making it as potential NO_2 active sites.[22,23] Meanwhile, isostructural MOFs (Cu_3-$(HHTQ)_2$ and $Ni_3(HHTQ)_2$) derived from multivalent metal ions were synthesized for comparison. The gas sensing response studies have confirmed that $Zn_3(HHTQ)_2$ exhibits a rapid and reversible response to NO_2, whereas Cu_3-$(HHTQ)_2$ and $Ni_3(HHTQ)_2$ display irreversible response even at 1 ppm NO_2 concentration. Additionally, we have explored the NO_2 sensing mechanism of $Zn_3(HHTQ)_2$ through a comprehensive analysis of spectroscopic characterizations and theoretical calculations. These findings indicate the feasibility of enhancing the gas sensing reversibility of 2D *c*-MOFs by employing only ligands with intrinsic gas sensing activity.

The HHTQ ligand was synthesized following well established protocols (Scheme S1).[24] $Zn_3(HHTQ)_2$ was synthesized through the coordination of zinc acetate dihydrate with the HHTQ ligand in a mixture of *N,N*-dimethylformamide (DMF)/deionized water (H_2O) at 85 °C (Figure 1a and Scheme S2). For comparison, $Cu_3(HHTQ)_2$ and $Ni_3(HHTQ)_2$ were prepared as well under same conditions.[25] $Zn_3(HHTQ)_2$ was thoroughly characterized using various analytical techniques. Analysis of the Fourier transform infrared (FT-IR) spectra (Figure S1) revealed a noticeable decrease in the stretching vibration of OH groups and new emergence of a distinct Zn–O stretching vibration band, confirming the successful coordination between HHTQ ligands and Zn ions. Elemental analysis was performed to determine the C, H, and N contents of $Zn_3(HHTQ)_2$, which closely matched the theoretical values. Additionally, nitrogen sorption measurement at 77 K was employed to evaluate the permanent porosity of Zn_3-$(HHTQ)_2$. As shown in Figure 1b, the Brunauer–Emmett–Teller (BET) surface area was calculated to be 403 $m^2 g^{-1}$ based on the N_2 adsorption branch ($P/P_0 < 0.15$), while the nonlocal density functional theory (NLDFT) method was employed to estimate the pore size distribution, revealing a dominant peak of approximately 2.1 nm, consistent with the theoretical diameter derived from simulated pore structures (2.2 nm).

The crystalline structure of $Zn_3(HHTQ)_2$ was elucidated using powder X-ray diffraction (PXRD) and high-resolution transmission electron microscopy (HRTEM). In the PXRD pattern of $Zn_3(HHTQ)_2$ (Figure 1c), a prominent diffraction peak at 4.02° corresponding to the (100) lattice plane was observed. Additionally, minor peaks at 8.10°, 10.72°, and 27.10°, attributed to the indices of 200, 210, and 001
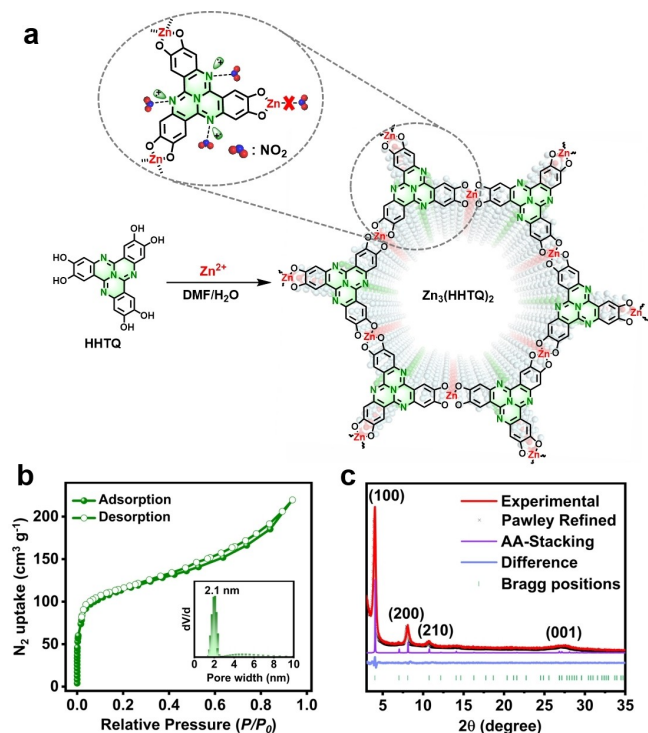
Figure 1. (a) Synthesis of $Zn_3(HHTQ)_2$. (b) N_2 sorption isotherm of $Zn_3(HHTQ)_2$ at 77 K (inset: pore size distribution). (c) Experimental and Pawley refined PXRD patterns of $Zn_3(HHTQ)_2$.

respectively, were also detected. Comparatively, the simulated PXRD pattern of $Zn_3(HHTQ)_2$ with AA stacking using Materials Studio software exhibited better agreement with the experimental data. Pawley refinement determined the *P6/M* space group with cell parameters $a = b = 25.12$ Å, $c = 3.32$ Å, $\alpha = \beta = 90°$, and $\gamma = 120°$ ($R_{wp} = 4.92\%$, $R_p = 4.52\%$). HRTEM images revealed distinct lattice fringes corresponding to (100) lattice plane throughout all crystallites, with $d_{100} = 2.20$ nm, consistent with the simulated structure (Figure S4a,b). Scanning electron microscope (SEM) images revealed a spherical morphology for $Zn_3(HHTQ)_2$ (Figure S4c,d).

To examine the valence state and chemical environment of the Zn transition metal centers, X-ray absorption fine-structure (XAFS) analysis was performed at the Zn K-edge. The X-ray absorption near-edge structure (XANES) spectrum of Zn in both $Zn_3(HHTQ)_2$ and reference samples (Zn and ZnO) exhibited a nearly identical white line peak for $Zn_3(HHTQ)_2$ compared to that of ZnO, indicating equivalent oxidation states of the Zn centers in $Zn_3(HHTQ)_2$ and ZnO (Figure 2a). Additionally, extended X-ray absorption fine-structure (EXAFS) analysis revealed similar oscillation patterns in k^2-weighted $\chi(k)$ spectra for both samples, indicating comparable coordination environments around the zinc atoms in both cases (Figure 2b). Fourier transform (FT) spectra derived from EXAFS oscillation k^2-weighted $\chi(k)$ data at the Zn K-edge provided insights into the neighboring atoms, such as oxygen and carbon, surrounding the zinc atoms (Figure 2c). Analysis of Figure S5 and Table S1 indicated a first coordinate peak at a distance of 1.80 Å corresponding to contributions from zinc-oxygen bonds, while the second peak at 2.21 Å was attributed to

zinc-carbon interaction. Notably, no peaks associated with zinc-zinc interactions was observed within this range. Consequently, the XANES and EXAFS analyses further corroborated the formation of zinc bis(dihydroxy) complex units within the framework of $Zn_3(HHTQ)_2$, consistent with its simulated structures. In addition, X-ray photoelectron spectroscopy (XPS) spectra also revealed the coexistence of C=O and C–O groups, indicating the presence of semi-quinone units upon partial oxidation (Figure 2d,f). Furthermore, the valence state of zinc ions was determined to be +2 (Figure 2e).

The thermal stability of $Zn_3(HHTQ)_2$ was evaluated using thermogravimetric analysis (TGA, Figure S7). $Zn_3(HHTQ)_2$ is thermally stable up to 258 °C. The TGA curve shows a weight loss of about 6% around 100 °C, indicating the presence of tightly bound water molecules (ca. four water molecules per structural unit) which is agreed well with the elemental analysis result. Additionally, the chemical stability of $Zn_3(HHTQ)_2$ was further examined by immersing the samples in common organic solvents, aqueous NaOH (0.5 M) and H_2SO_4 (0.5 M) for 3 days. All the samples maintained their crystallinity and chemical constitution after these treatments except in the acidic condition, as revealed by the PXRD patterns and FT-IR spectra (Figure S8). The decent thermal and chemical stability of $Zn_3(HHTQ)_2$, making it a promising material for gas sensing.

NO_2 is a notorious global pollutant due to its potent toxicity even at low concentrations.[23,26] The utilization of 2D *c*-MOFs as NO_2 sensing materials has shown remarkable performance.[12–13,18–19] However, the reported response mechanism of 2D *c*-MOFs to NO_2 typically involves redox reactions between metal ions and NO_2 gas, resulting in
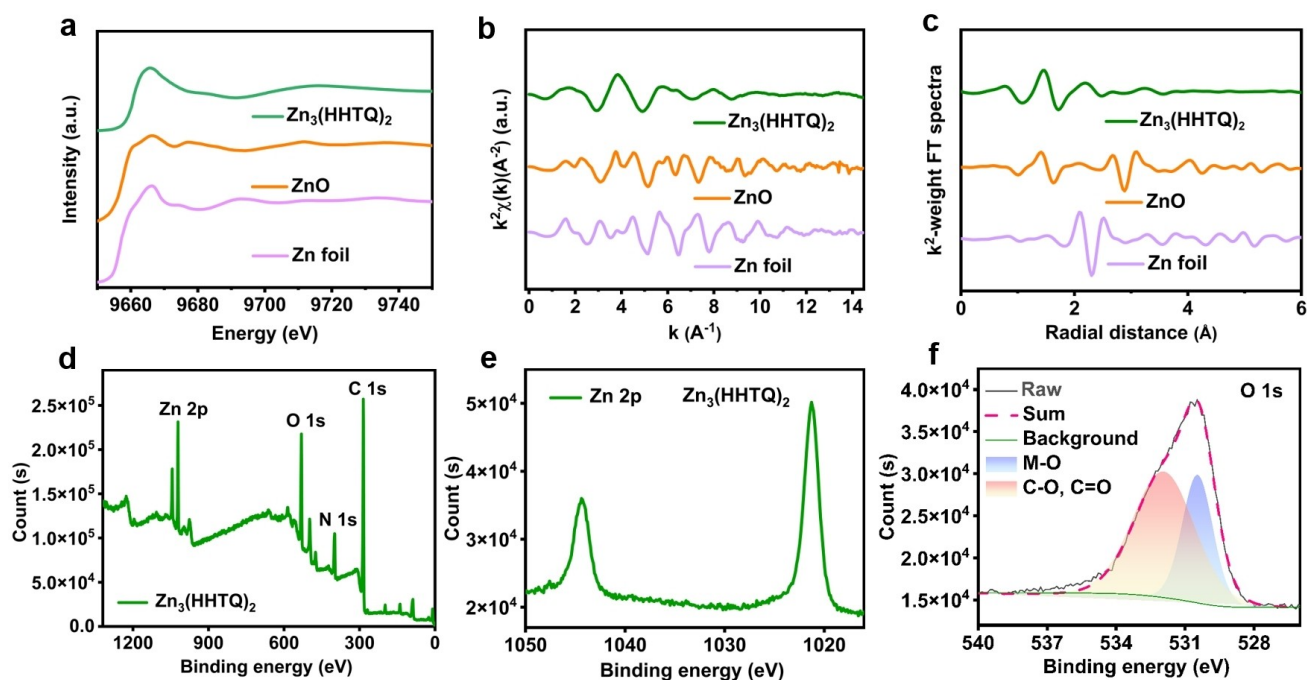

Figure 2. (a) XANES spectra of Zn K-edge and EXAFS oscillations, (b) $k^2 \chi(k)$ and (c) k^2-weighted FT spectra for $Zn_3(HHTQ)_2$, the standard Zn foil, and ZnO. (d) Survey scan XPS profiles, (e) high resolution Zn 2p and (f) O 1s XPS profiles of $Zn_3(HHTQ)_2$.

diminished stability as a NO$_2$ sensing material and constraining its practical applications.[14–17] Considering the innocent redox activity of Zn^{2+} towards NO$_2$, together with the potential reactivity sites (C=N) from the HHTQ ligand, we strategically employed Zn$_3$(HHTQ)$_2$ for NO$_2$ sensing with the aim of improving the stability of NO$_2$ sensing in 2D c-MOFs. Zn$_3$(HHTQ)$_2$ was deposited onto interdigitated electrodes using a drop-casting technique, and the current response of the device was recorded under a NO$_2$ atmosphere. Comparative evaluations were conducted with Cu$_3$-(HHTQ)$_2$ and Ni$_3$(HHTQ)$_2$ employing analogous methodologies. As shown in Figure 3a–c, the response characteristics of M$_3$(HHTQ)$_2$ (M=Zn, Cu or Ni) were investigated over NO$_2$ concentrations ranging from 1 to 10 ppm. Zn$_3$(HHTQ)$_2$ exhibited remarkable response-recovery ability with the response coefficient of variation (CV) only 2.6% over five consecutive cycles (3 ppm), highlighting its exceptional repeatability and reliability (Figures 3a,d and S10). In contrast, Cu$_3$(HHTQ)$_2$ and Ni$_3$(HHTQ)$_2$ displayed irreversible response and recovery at a low concentration of 3 ppm NO$_2$ with significantly larger response CV of 11.9% and 24.8% respectively over the same number of cycles, indicating their poorer repeatability and reliability (Figures 3b–e and S10). Furthermore, after 20 minutes of air purging, Cu$_3$(HHTQ)$_2$ and Ni$_3$(HHTQ)$_2$ exhibit only 59.8% and 66.7% recovery, respectively, whereas Zn$_3$(HHTQ)$_2$ achieves complete recovery in just 10 minutes (Figures 3e and S11). Subsequently, we conducted a comprehensive investigation into the NO$_2$ sensing of Zn$_3$(HHTQ)$_2$. The log-log plot of Zn$_3$(HHTQ)$_2$ response concentration demonstrated excellent linearity within the 1–10 ppm range (Figure S12). Utilizing linear equation fitting and setting the response value to 10%, a theoretical detection limit (LOD)

of 0.269 ppm was calculated. Furthermore, the response time (t_{res}) of Zn$_3$(HHTQ)$_2$ to 3 ppm NO$_2$, representing the time required for the current to reach 90% of the maximum signal, was evaluated (Figure S11a). The t_{res} of Zn$_3$(HHTQ)$_2$ (2.2 min) was relatively short, which could be attributed to the rapid adsorption of NO$_2$ facilitated by the active sites distributed along the densely arranged ligands within the one-dimensional channels. Additionally, the selectivity of Zn$_3$(HHTQ)$_2$ for NO$_2$ detection was assessed by exposing it to 12 different interfering gases at a concentration of 100 ppm for 3 minutes (Figure 3f). Notably, Zn$_3$(HHTQ)$_2$ exhibited a minimal response (below 10%) to these interfering gases, underscoring its excellent selectivity in distinguishing NO$_2$ from common interfering gases.

To delve deeper into the structural changes induced by NO$_2$ sensing, the PXRD patterns and N$_2$ adsorption-desorption isotherms of M$_3$(HHTQ)$_2$ (M=Zn, Cu or Ni) before and after exposure to NO$_2$ were examined. As shown in Figure S13, the crystallinity and BET surface area of Zn$_3$(HHTQ)$_2$ remained nearly unchanged before and after NO$_2$ sensing. In contrast, Cu$_3$(HHTQ)$_2$ and Ni$_3$(HHTQ)$_2$ displayed an obvious reduction in both crystallinity and BET surface area after NO$_2$ exposure (Figures S14, S15). These experimental results have preliminarily validated our hypothesis that the active sites responsible for NO$_2$ sensing in Cu$_3$(HHTQ)$_2$ and Ni$_3$(HHTQ)$_2$ are primarily located on the metal ions. These metal ions possess a strong affinity for NO$_2$, impeding its release from the framework during the NO$_2$ sensing process. Additionally, the redox process between the metal ions and NO$_2$ disrupts the coordination bonds in the 2D c-MOF materials, resulting in an irreversible response to NO$_2$. In contrast, the Zn ions in Zn$_3$-(HHTQ)$_2$, lacking inherent redox activity, demonstrate a
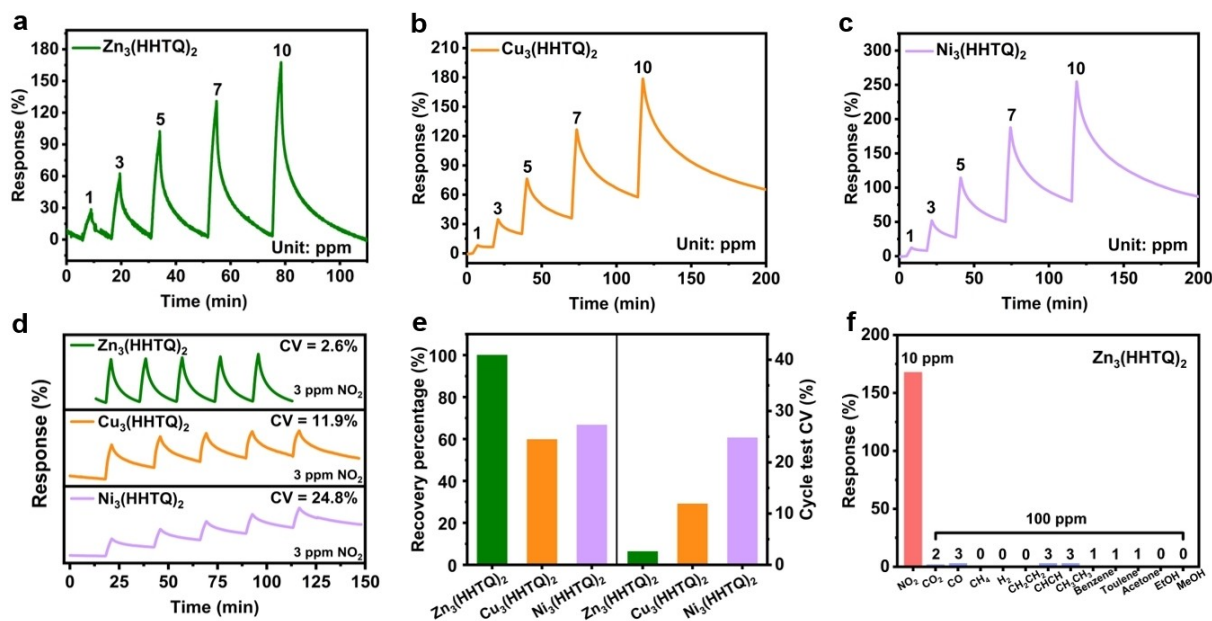
Figure 3. Gas-sensing performances of the devices at room temperature. Dynamic response curves of (a) Zn$_3$(HHTQ)$_2$, (b) Cu$_3$(HHTQ)$_2$ and (c) Ni$_3$(HHTQ)$_2$ towards 1–10 ppm NO$_2$. (d) Response-recovery cycle plots and (e) Coefficient of variation for cycle testing (orange), recovery percentage (green) of Zn$_3$(HHTQ)$_2$, Cu$_3$(HHTQ)$_2$, Ni$_3$(HHTQ)$_2$ towards 3 ppm NO$_2$. (f) Response ability of Zn$_3$(HHTQ)$_2$ toward different gas.

*Angew. Chem. Int. Ed.* **2024**, e202408189 (4 of 6)

© 2024 Wiley-VCH GmbH

strong response-recovery ability, and thus the response sites are predominantly concentrated on the unsaturated C=N bonds of the ligands.

To further validate our hypothesis, we performed a computational analysis of the adsorption energy (E_{ad}) between NO_2 molecules and potential active sites on M_3-$(HHTQ)_2$ (M = Zn, Cu or Ni, Figure 4a,b). The geometrically optimized models of NO_2 adsorption on the active sites of $M_3(HHTQ)_2$ are shown in Figures S16–S20, showcasing both top and side views. Notably, the Cu and Ni ions exhibited higher adsorption energies of −0.76 and −0.87 eV, respectively, indicating a dominant role in NO_2 adsorption (Figure 4b). In contrast, the Zn ions displayed much lower adsorption energy of −0.50 eV, with a small difference in adsorption energy between the N1 and N2 active sites. To gain deeper insights into the response mechanism, we employed XPS and XAFS spectra to examine the changes before and after NO_2 exposure. As shown in Figure S21, exposure to NO_2 leads to an increase in Cu^{2+}/Ni^{3+} ions (Orange region) within $Cu_3/Ni_3(HHTQ)_2$, accompanied by a reduction in Cu^+/Ni^{2+} ion population (Blue region).[13,27–28] The above results, combined with the adsorption energy findings and the behavior of $Cu_3/Ni_3(HHTQ)_2$ towards NO_2, implies that the enhanced adsorption energy between Cu/Ni ions and NO_2 within $Cu_3/Ni_3(HHTQ)_2$ hinders the release of NO_2 from its framework. Additionally, the redox process occurring between Cu/Ni ions and NO_2 disrupts coordination bonds within this material, resulting in an irreversible

response towards NO_2. In contrast, as shown in Figure 4c and Figure S22, the XPS and XAFS results of $Zn_3(HHTQ)_2$ before and after NO_2 sensing demonstrate no alteration in the oxidation state or coordination number of Zn ions. Notably, the N 1S spectra revealed a reduction in the quantity of C=N bonds within $Zn_3(HHTQ)_2$, accompanied by an increase in $–N^{•+}–$ (Figure 4d, Magenta region).[22] Considering its response behavior and calculated adsorption energy, we propose that the active sites responsible for the response in $Zn_3(HHTQ)_2$ predominantly reside on unsaturated C=N bonds, thereby exhibiting exceptional response-recovery performance. Based on these findings, we propose the following rational mechanism of $Zn_3(HHTQ)_2$ for NO_2 sensing: upon exposure to NO_2, rapid adsorption of NO_2 molecules occurs within $Zn_3(HHTQ)_2$. Simultaneously, as a potent electron acceptor, NO_2 molecules interact with the unsaturated C=N bonds through redox interactions or coordination, resulting in the formation of $–N^{•+}–$ and subsequent changes in conductivity. Upon removal of NO_2 from $Zn_3(HHTQ)_2$, the trapped electrons are released back into the $Zn_3(HHTQ)_2$, causing the current recovery of the sensor (Figure 4e).[22]

In summary, this study introduces an effective strategy to enhance the stability and recyclability of 2D *c*-MOF sensing materials. By engineering sensing active sites onto bridging ligands instead of metal nodes, we have developed $Zn_3(HHTQ)_2$, a 2D *c*-MOF that exhibits a rapid and reversible response to NO_2. This contrasts with the irreversible sensing behaviors of $Cu_3(HHTQ)_2$ and $Ni_3(HHTQ)_2$, which utilize metal-centric sites, highlighting the pivotal role of ligand-based design in dictating MOF gas sensing properties. The ligand-centered approach significantly improves sensor reversibility, reduces recovery times, and maintains structural integrity. These findings highlight the significance of ligand engineering in MOF-based gas sensing materials and offer new possibilities for further advancements in this field.
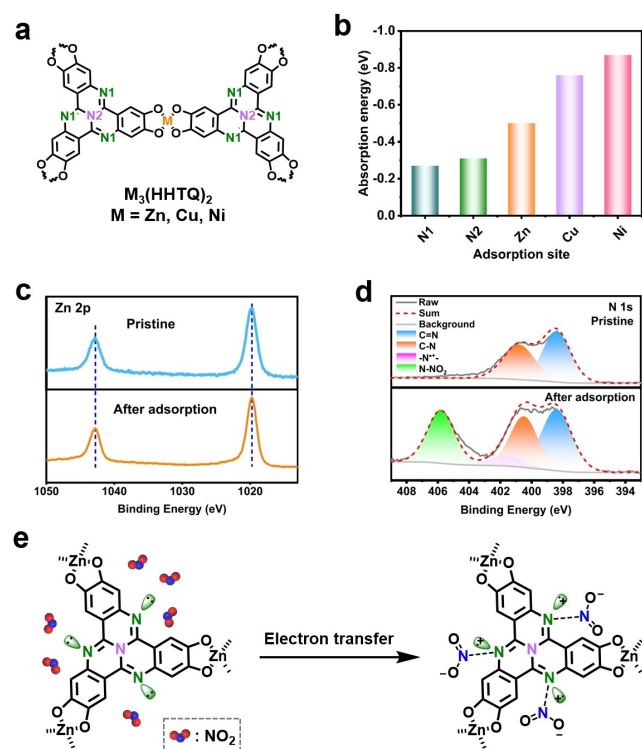
Figure 4. (a) The sites for adsorption energy calculations in M_3-$(HHTQ)_2$. (b) Adsorption energies of $M_3(HHTQ)_2$ for NO_2. (c) Zn 2p and (d) N 1s XPS spectra of $Zn_3(HHTQ)_2$ in the pristine state and after NO_2 adsorption. (e) Proposed NO_2 sensing process of $Zn_3(HHTQ)_2$.

Angew. Chem. Int. Ed. **2024**, e202408189 (5 of 6)

© 2024 Wiley-VCH GmbH

[1] M. Wang, R. Dong, X. Feng, *Chem. Soc. Rev.* **2021**, *50*, 2764–2793.

[2] J. Liu, X. Song, T. Zhang, S. Liu, H. Wen, L. Chen, *Angew. Chem. Int. Ed.* **2021**, *60*, 5612–5624.

[3] X. Yan, X. Su, J. Chen, C. Jin, L. Chen, *Angew. Chem. Int. Ed.* **2023**, *62*, e202305408.

[4] G. Chakraborty, I.-H. Park, R. Medishetty, J. J. Vittal, *Chem. Rev.* **2021**, *121*, 3751–3891.

[5] L. Lüder, A. Gubicza, M. Stiefel, J. Overbeck, D. Beretta, A. Sadeghpour, A. Neels, P. N. Nirmalraj, R. M. Rossi, C. Toncelli, M. Calame, *Adv. Electron. Mater.* **2021**, *8*, 2100871.

[6] L. Jiang, H. Wang, Z. Rao, J. Zhu, G. Li, Q. Huang, Z. Wang, H. Liu, *J. Colloid Interface Sci.* **2022**, *622*, 871–879.

[7] C. A. Downes, S. C. Marinescu, *ChemSusChem* **2017**, *10*, 4374–4392.

[8] K. W. Nam, S. S. Park, R. Dos Reis, V. P. Dravid, H. Kim, C. A. Mirkin, J. F. Stoddart, *Nat. Commun.* **2019**, *10*, 4948.

[9] L. S. Xie, G. Skorupskii, M. Dinca, *Chem. Rev.* **2020**, *120*, 8536–8580.

[10] J. Liu, Y. Chen, X. Feng, R. Dong, *Small Structures* **2022**, *3*, 2100210.

[11] C. Park, J. W. Baek, E. Shin, I.-D. Kim, *ACS Nanosci. Au* **2023**, *3*, 353–374.

[12] X. Su, Z. Zhong, X. Yan, T. Zhang, C. Wang, Y.-X. Wang, G. Xu, L. Chen, *Angew. Chem. Int. Ed.* **2023**, *62*, e202302645.

[13] P. Chen, X. Su, C. Wang, G. Zhang, T. Zhang, G. Xu, L. Chen, *Angew. Chem. Int. Ed.* **2023**, *62*, e202306224.

[14] A. Aykanat, Z. Meng, R. M. Stolz, C. T. Morrell, K. A. Mirica, *Angew. Chem. Int. Ed.* **2022**, *61*, e202113665.

[15] Z. Meng, A. Aykanat, K. A. Mirica, *J. Am. Chem. Soc.* **2019**, *141*, 2046–2053.

[16] M. G. Campbell, D. Sheberla, S. F. Liu, T. M. Swager, M. Dincă, *Angew. Chem. Int. Ed.* **2015**, *54*, 4349–4352.

[17] M. G. Campbell, S. F. Liu, T. M. Swager, M. Dincă, *J. Am. Chem. Soc.* **2015**, *137*, 13780–13783.

[18] H. Lim, H. Kwon, H. Kang, J. E. Jang, H.-J. Kwon, *Nat. Commun.* **2023**, *14*, 3114.

[19] Y. Yue, P. Cai, X. Xu, H. Li, H. Chen, H.-C. Zhou, N. Huang, *Angew. Chem. Int. Ed.* **2021**, *60*, 10806–10813.

[20] Y. Lin, W.-H. Li, Y. Wen, G.-E. Wang, X.-L. Ye, G. Xu, *Angew. Chem. Int. Ed.* **2021**, *60*, 25758–25761.

[21] D. An, L. Chen, Y. Liang, J. Hou, J. Chen, *J. Mater. Chem. A* **2024**, *12*, 38–58.

[22] B. Feng, X. Chen, P. Yan, S. Huang, C. Lu, H. Ji, J. Zhu, Z. Yang, K. Cao, X. Zhuang, *J. Am. Chem. Soc.* **2023**, *145*, 26871–26882.

[23] H. Jiang, L. Cao, Y. Li, W. Li, X. Ye, W. Deng, X. Jiang, G. Wang, G. Xu, *Chem. Commun.* **2020**, *56*, 5366–5369.

[24] J.-H. Dou, M. Q. Arguilla, Y. Luo, J. Li, W. Zhang, L. Sun, J. L. Mancuso, L. Yang, T. Chen, L. R. Parent, G. Skorupskii, N. J. Libretto, C. Sun, M. C. Yang, P. V. Dip, E. J. Brignole, J. T. Miller, J. Kong, C. H. Hendon, J. Sun, M. Dincă, *Nat. Mater.* **2021**, *20*, 222–228.

[25] J. Liu, D. Yang, Y. Zhou, G. Zhang, G. Xing, Y. Liu, Y. Ma, O. Terasaki, S. Yang, L. Chen, *Angew. Chem. Int. Ed.* **2021**, *60*, 14473–14479.

[26] J. Song, J. Baek, J. Cho, T. Kim, M. Kim, H. S. Kim, J. Mun, S.-W. Kang, *Small Structures* **2023**, *4*, 2200392.

[27] G.-Y. Hou, Y.-Y. Xie, L.-K. Wu, H.-Z. Cao, Y.-P. Tang, G.-Q. Zheng, *Int. J. Hydrogen Energy* **2016**, *41*, 9295–9302.

[28] R. Shen, X. Li, X. Xia, H. Liang, G. Wu, Y. Liu, C. Cheng, G. Du, *Chin. Sci. Bull.* **2012**, *57*, 2087–2093.

Communications

X. Yan, J. Chen, X. Su, J. Zhang, C. Wang,
H. Zhang, Y. Liu,* L. Wang, G. Xu,*
L. Chen* ——————————— **e202408189**

Redox Synergy: Enhancing Gas Sensing
Stability in 2D Conjugated Metal–Organic
Frameworks via Balancing Metal Node and
Ligand Reactivity
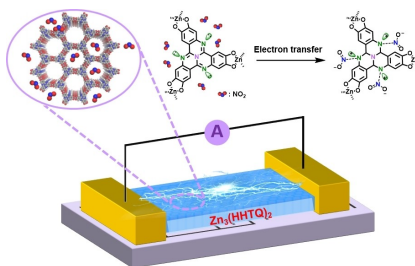
A redox innocent zinc metal center-based 2D *c*-MOF, $Zn_3(HHTQ)_2$, with ligand-centered sensing active sites has been developed for NO_2 sensing, which demonstrates excellent cycling stability and high selectivity without compromising the coordination bonds.

SPACE RESERVED FOR IMAGE AND LINK

Share your work on social media! *Angewandte Chemie* has added Twitter as a means to promote your article. Twitter is an online microblogging service that enables its users to send and read short messages and media, known as tweets. Please check the pre-written tweet in the galley proofs for accuracy. If you, your team, or institution have a Twitter account, please include its handle @username. Please use hashtags only for the most important keywords, such as #catalysis, #nanoparticles, or #proteindesign. The ToC picture and a link to your article will be added automatically, so the **tweet text must not exceed 250 characters**. This tweet will be posted on the journal's Twitter account (follow us @angew_chem) upon publication of your article in its final (possibly unpaginated) form. We recommend you to re-tweet it to alert more researchers about your publication, or to point it out to your institution's social media team.

Please check that the ORCID identifiers listed below are correct. We encourage all authors to provide an ORCID identifier for each coauthor. ORCID is a registry that provides researchers with a unique digital identifier. Some funding agencies recommend or even require the inclusion of ORCID IDs in all published articles, and authors should consult their funding agency guidelines for details. Registration is easy and free; for further information, see http://orcid.org/.

Dr. Xiaoli Yan
Jie Chen
Xi Su
Jingwen Zhang
Chuanzhe Wang
Hanwen Zhang
Prof. Yi Liu
Prof. Lei Wang
Prof. Gang Xu
Prof. Long Chen http://orcid.org/0000-0001-5908-266X